Major Results from Wendelstein 7-AS Stellarator

F. Wagner, R. Burhenn, F. Gadelmeier, J. Geiger, M. Hirsch, H. P. Laqua, A. Weller, A. Werner, S. Bäumel, J. Baldzuhn, R. Brakel, A. Dinklage, P. Grigull, M. Endler, V. Erckmann, H. Ehmler, Y. Feng, R. Fischer, L. Giannone, H.-J. Hartfuss, A. Hermann, D. Hildebrandt, E. Holzhauer, Y. Igitkhanov, R. Jänicke, M. Kick, A. Kislyakov 1), A. Kreter 2), J. Kisslinger, T. Klinger, S. Klose, J. P. Knauer, R. König, G. Kühner, H. Maassberg, K. McCormick, D. Naujoks, H. Niedermeyer, C. Nührenberg, E. Pasch, N. Ramasubramanian, N. Rust, E. Sallander, F. Sardei, M. Schubert, H. Thomsen, F. Volpe, U. Wenzel, H. Wobig, E. Würsching, M. Zarnstorff 3), S. Zoletnik 4), and the W7-AS Team

Max-Planck-Institut für Plasmaphysik, EURATOM Association, 85748 Garching, 17491 Greifswald, Germany

1) IOFFE-Institute, St. Petersburg, Russia
2) Forschungszentrum Jülich, EURATOM Association, Jülich, Germany
3) Princeton Plasma Physics Laboratory, Princeton, USA
4) KFKI-RMKI, EURATOM Association, Budapest, Hungaria

e-mail contact: fritz.wagner@ipp.mpg.de

Abstract. This paper is a summary of some of the major results from W7-AS stellarator and addresses - electron Bernstein wave heating - beach-wave heating - aspects of the partial optimisation of the magnetic design - the island divertor operation and the modelling of the results with the EMC3/EIRENE code - confinement issues with emphasis on the differences to tokamaks (isotope effect, density scaling, lack of profile resilience) - some of the H-mode findings (operational windows, transition physics) - the characteristics of the High-Density-H-mode - stability issues (GAEs, ELMs), and - operational limits.

1. Introduction

After nearly 14 years with 56953 discharges W7-AS has suspended operation. The device is now mothballed. The development of the Wendelstein stellarator line will continue with the W7-X device. The major goals of W7-AS were - to test the modular coil concept, - to demonstrate the effectiveness of the first steps toward an optimised stellarator design, and - to develop an exhaust concept based on the natural island chain which forms the plasma boundary. W7-AS has contributed to all areas of stellarator and fusion research. This paper gives a brief summary of some of the most relevant results.

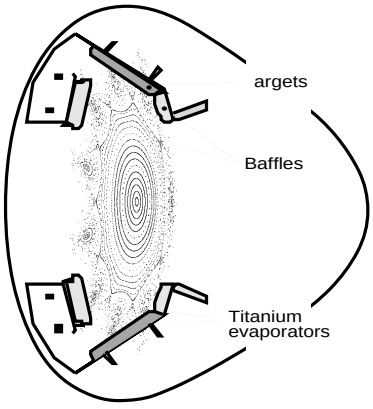

FIG.1. Cross-section in the elliptical plane: vacuum flux surfaces and two divertor modules

2. Device Characteristics

W7-AS is a flexible system comprising 45 modular coils, which produce both toroidal and poloidal field components with dominant l=2 and l=3 poloidal components. An additional set of toroidal field coils enables change of rotational transform; five separately operated modular coils at the corners of the pentagon-like shaped system with n=5 toroidal symmetry allow variation of the toroidal mirror ratio; the plasma position could be changed with vertical field coils; an ohmic system was used to modify rotational transform, to study current driven instabilities, or to compensate the bootstrap current (generally, this was the mode of operation). Five in-vessel control coil pairs, which allowed to change the $B_{5,m}$ field spectrum,

were used to vary the edge island size (and along with it the connection length) employed for divertor operation.

W7-AS pioneered the island divertor for the low-shear Wendelstein line. Fig. 1 shows a poloidal cross-section with cuts through the upper and lower divertor modules. Five divertor module pairs (top-bottom) were installed at the 5 toroidal positions with elliptical plasma cross-section. The inserts provided the target and baffle plates and gave room for fairly closed divertor chambers. Diversion occurred with the edge islands, preferentially via the 5/m (m=8, 9, 10) island chains. The strike points were defined by the intersection of the outer island separatrix with the target plates. The divertor gave access to plasmas with high density at quasi-steady-state conditions, good energy and low impurity confinement properties, large radiation from the plasma edge, and partial detachment. The scrape-off layer and the discrete divertor modules established a 3-D edge geometry, which was modelled by the 3-D edge transport code EMC3/EIRENE /1/.

Plasma heating was done with ECRH (70 GHz, 140 GHz, < 2.4 MW absorbed power), NBI [< 2.8 MW absorbed power; in the last phase with all-co (or all-ctr) orientation], and ICRH (up to 1 MW antenna power). OH power could be neglected in all heating scenarios.
ECRH was operated under conventional O- and X-mode conditions for heating and current drive. But high-density operation necessitated the development of ECRF heating beyond the conventional cut-off conditions on the basis of the known OXB heating scheme /2/. The high-density plasma core was ultimately heated by the electrostatic Bernstein wave. The heating efficiency (~80%) was comparable to other hf-heating methods. The pre-requisites for successful heating at high efficiency were provided at W7-AS viz. steep edge density gradients ($L_n \approx$ 0.5–1 cm) and a low density fluctuation level (≈10%) for effective O- to X-mode coupling and a high plasma density ($n_e > 2.5 \times 10^{20}$ m^{-3} for 140 GHz) for effective mode conversion. Bernstein wave heating could be demonstrated up to the fourth harmonic (140 GHz at 1.1 T). An example of OXB heating is shown in Fig. 2. This scenario was also used for current drive and heat-wave experiments. The inverse process was used for temperature profile measurements at ultra-high densities via electron-Bernstein-wave emission. A detailed account of the ECRH studies is given in /3/.

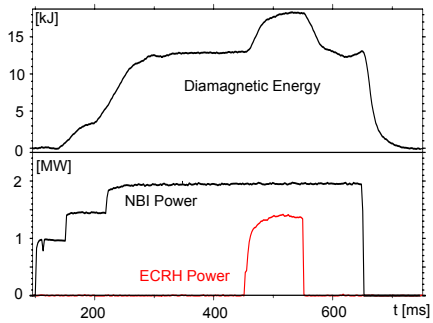

FIG.2. Increase of plasma energy during electron Bernstein wave heating (140 GHz) at a density of 3.5 10^{20} m^{-3} and a magnetic field of 2.12 T. Target plasma heating is with NBI.

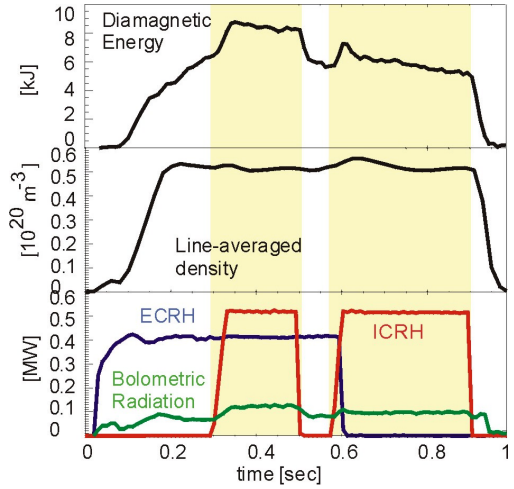

FIG. 3. Diamagnetic energy of an ECRH/ICRH heated plasma. An ICRH heating pulse in the beach-wave mode is applied from 0.3-0.5 s. After 0.6 s the plasma is maintained by beach-wave ICRF heating only.

Different ICRH heating schemes with sufficiently high single pass absorption were successfully employed on W7-AS, such as 2nd harmonic heating, minority heating and mode conversion /4/. Moreover, the toroidal variation of the magnetic field was used for beach-wave heating. Fig. 3 shows an example of ICRF beach-wave heating at an antenna power of 0.5 MW. The heating efficiency is ≈ 80 %.

3. Stellarator Specific Issues

3.1. Partial Optimisation

The geometry of W7-AS has been partially optimised. The parallel currents were reduced in W7-AS in comparison to an equivalent classical l=2 stellarator ($\langle j_{\|,AS}^2 \rangle / \langle j_{\|,l=2}^2 \rangle \sim 0.5$). As a result the equilibrium is improved for high ß due to the reduced displacement of the magnetic axis. The experimental analysis of the Shafranov shift as a function of <ß> (via SX tomography) has fully confirmed this design property. Fig. 4 shows the variation of the magnetic axis R_{axis} with <ß> up to 3.4% and compares the experimental data with the result from free-boundary equilibrium calculations (NEMEC, solid line). Good agreement is observed.

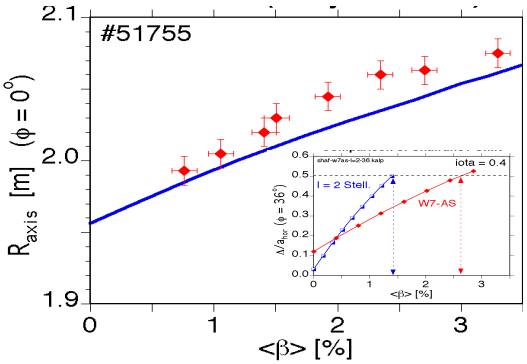

FIG. 4. Shift of the magnetic axis with <ß> (exp. data and NEMEC calculation.); insert: relative Shafranov shift in W7-AS compared to a classical l=2 stellarator

The impact of the partial optimisation on neo-classical effects is more difficult to demonstrate. The measured (tokamak-like) bootstrap current is in agreement with the neo-classical calculations (DKES /5/). The neo-classical transport, which governs the plasma core in the LMFP regime, is strongly affected by the ambipolar radial electric field, which may mask the potential role of the partial orbit optimisation. Specifically, the development of the electron root (driven by non-thermal fluxes from ECRH) with strongly positive electric field gives rise to low core transport and thus high electron temperatures displaying the profile characteristics of internal transport barriers. A case is shown in Fig. 5. In the radial range from r < 5cm, the ambipolar field was measured to be strongly positive (+400 V/cm); beyond this radius, the ion root is established. The strong positive electric field reduces the neo-classical electron heat diffusivity from 10-20 m^2/s to 2-5 m^2/s. The T_e-gradients in the inner zone are remarkable: $\nabla T_e \sim 1$keV/cm, $R/L_{Te} = 60$; in the outer zone: $R/L_{Te} = 40$ (major radius to T_e-gradient length).

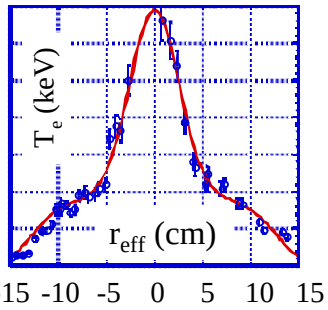

FIG.5. T_e-profile with 2 MW of central ECRH. $n_e = 2\ 10^{19}\ m^{-3}$

3.2. Fast Particle Confinement

In stellarators, the 3-D magnetic configuration can lead to particles on unconfined trajectories. The losses are specifically severe for energetic particles. In the optimisation strategy, a remedy is to locally increase |B| in zones of large curvature. Also in the design of W7-X, this effect is embedded (besides the improved fast particle confinement via the magnetic well at higher ß). With the use of a fast ion loss detector, the confinement of fast ions, injected by a radial neutral injector, was investigated for different mirror ratios along the toroidal direction. Fig. 6 shows the loss current as a function of the mirror ratio. Low field in the region of large curvature leads to enhanced ion losses; high fields in this region give rise to low fluxes.

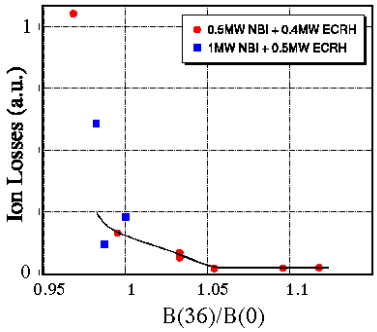

FIG. 6. Ion losses depending on the toroidal mirror ratio; the curve guides the eye.

3.3. Low Global Shear

The Wendelstein stellarator line has low shear, S, in the vacuum field. The basic design idea is to avoid low-order rationals inside the plasma and to utilise the empirically observed good confinement in the proximity of low-order rationals. Most consequential, this aspect is exploited in W7-X. The feature of low-shear has a concept-specific impact on confinement, which – as a result - strongly depends on ι (Fig. 7). In the neighbourhood of

low-order rationals, the confinement can be good; these are the ranges where generally the confinement studies are done. In these windows also transitions into improved regimes like the H-NBI regime (close to ι =1/3) or the H* mode (around ι =1/2) occur. The development of the H-mode displays a fine structure in ι to be discussed later. As a consequence, there are three levels of confinement: - the standard confinement in the neighbourhood of ι = 1/3 and 1/2 (these are the ranges, where the confinement database is established); - the low, sub-standard level between the maxima; - improved confinement regimes (limited to specific ι-windows).

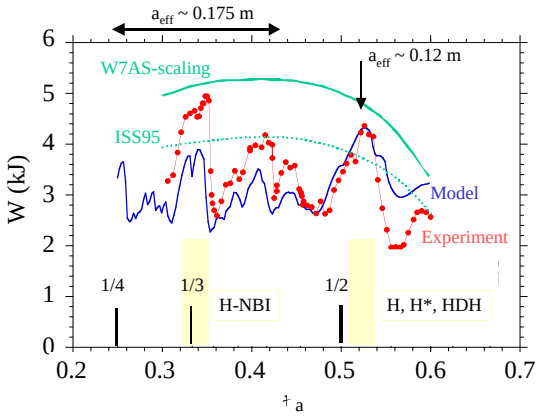

FIG. 7. Energy content vs. ι; the experimental results are compared with modelling and the expectations from two confinement scalings (the W7-AS and the ISS95 – scaling /6/). Windows with improved confinement are indicated; toward higher ι, the plasma cross-section is reduced. The effective plasma radii are indicated.

The confinement results of Fig. 7 are compared with a heuristic model of electron energy transport. Three components are considered:– a background of neo-classical transport, -a term subsuming electrostatic turbulence and, on top of it, -a local contribution of high turbulence, attributed to rationals with an amplitude, which depends on n and m, the toroidal and poloidal mode numbers, and with a radial extent around the rationals, which depends on S. Because of the complex interplay of confinement, pressure, and internal currents with ι, the behaviour is highly non-linear. This is seen experimentally but also born out by the model. Also bifurcations can occur. These were also successfully predicted by the model.

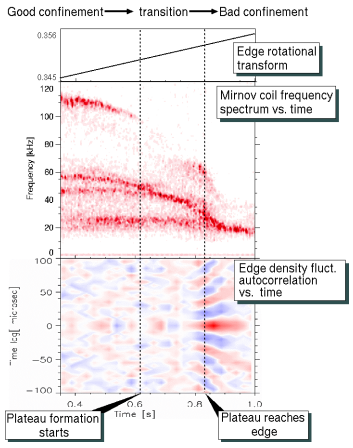

FIG. 8. a) ι-ramp; b) frequency spectra of MHD; c) auto-correlation of edge turbulence measured with the Li-beam.

The spatially non–resolved turbulence level (measured by micro-wave or CO_2 scattering) increases at the transition from "good" to "bad" ι - windows. Only indirectly, from slow ι-scans, the turbulence can be attributed to specific zones inside the plasma associated with rationals. Localised MHD modes move radially toward the outside and slow down when ι is increased; they merge in frequency whereas the T_e-profile develops pleateaus and finally they are detected at the edge by the local Li-beam diagnostics. As soon as the plateaus reach the plasma edge, the confinement is low. Fig. 8 shows the turbulence characteristics in a case where the variation of ι induces a transition from "good" to "bad" confinement.

The MHD stability of a low-shear device depends on the magnetic well. Under normal operational conditions, the vacuum field geometry has a magnetic well typically of 1-1.5%. Such a system shows a strong additional stabilising effect due to diamagnetic currents, which develop toward high ß. Fig 9 shows a high-ß NBI heated discharge with MHD activity, which comprises two components: a beam-pressure driven Alfvén-wave and a thermal pressure driven m=2 MHD mode located at the ι=0.5 resonance. Toward high-ß, both components disappear: the Alfvén mode is stabilised by the increasing thermal ß, the thermal pressure driven mode is stabilised possibly by the deepening magnetic well and the

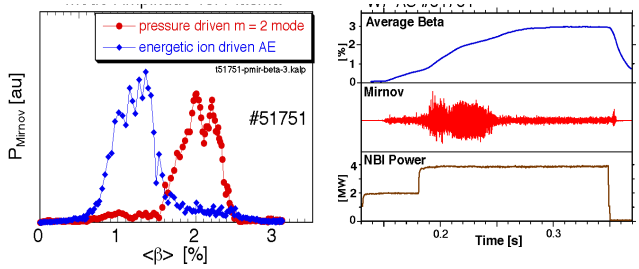

FIG.9. Mode amplitudes versus ß; time traces of a high ß-discharge.

radial shift of the resonance toward more stable conditions. At the highest ß, the discharge becomes quiescent again.

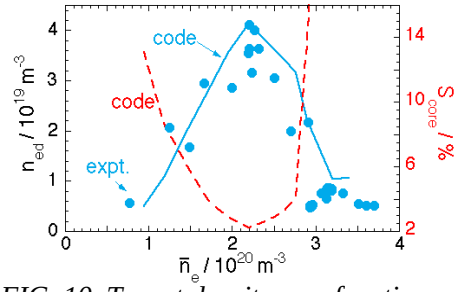

FIG. 10. Target density as a function of line averaged plasma density. The experimental results are compared with modelling. Dashed curve: the contribution of the ionisation source in the core.

4. Island Divertor Operation

Island divertor configurations were studied at high density generally with NBI. The power fluxes across the separatrix are up to 0.25 MW/m^2 and match those of prototypical poloidal field divertor devices. The P/R values are about 1.5 MW/m. The divertor allowed the density to be increased from 2.5 10^{20}m^{-3} (only transiently with limiter) to 4 10^{20}m^{-3}, maintained quasi steady state. In this density range, most of the recycling neutrals are ionised in the scrape-off layer except at detachment (see core ionisation rate in Fig. 10). Power is radiated mostly via low ionisation states of oxygen and carbon from the target plate material. However, strong flux enhancement under high-recycling conditions is not observed and also not expected. Unlike the poloidal field divertor, the main traits of the island divertor are given by the strong perpendicular transport of parallel momentum. The flow to the target plate is impeded even at high SOL temperatures and without intense neutral gas interaction. Fig. 10 shows edge parameters as a function of main plasma density. At low density, there is a linear relation between divertor and plasma density; at a main plasma density of 2.2 10^{20} m^{-3} and a divertor density of 0.4 10^{20} m^{-3} rollover appears followed by detachment without an intermediate high-recycling regime. The EMC3/EIRENE code reproduces the results well.

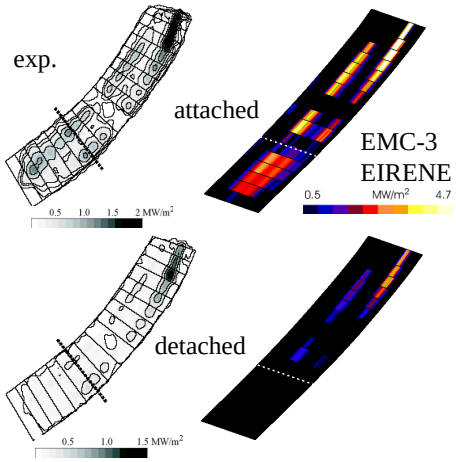

FIG. 11. Thermographic measurements of the power flux at the target plates under attached and detached conditions; EMC3/EIRENE modelling of the results.

In Fig. 11 the power deposition at the target plates under attached and detached conditions are compared. Detachment is partial and those sectors remain attached, which are magnetically connected to the mid-plane of the plasma at the outside (flux-surface compression leads to high local heat flux at the mid-plane outside whereby carbon radiation cools the plasma at the cold inside). Detachment is restricted in parameter space and it requires the island divertor: if the separatrix-target plate distance is reduced to less than 2 cm, stable partial detachment is replaced by impurity induced plasma collapse.

The EMC3/EIRENE modelling reproduces qualitatively the experimental findings like the edge parameter development with the onset of detachment (Fig.10), drift effects, the location of the hot spots (Fig. 11), the jump in carbon radiation at the onset of detachment and the propagation of the ionisation front from the target to the separatrix. A detailed account of the divertor studies is given in /7/.

5. Turbulent Transport and Confinement

The outer plasma zone, which determines the energy confinement time, is governed by electrostatic turbulence (in the “good” iota ranges). The confinement time observed in W7-AS is comparable to that of tokamaks and reproduces its main features like power degradation and bifurcations – specifically to the H-mode. W7-AS was the first “non-tokamak” to operate with the H-mode. Fig. 12 compares experimental τ_E values to those expected from stellarator and tokamak scaling. The data are taken from discharges at operational limits (highest temperatures, density, ß, confinement...). To allow comparison, ι, B and the geometry are rephrased into an effective plasma current; the average elongation of W7-AS is 1.9. There is an obvious similarity in anomalous tokamak and stellarator confinement. Both are set by

gradient driven turbulence. The good agreement seems to justify the replacement of current I_p by B and geometrical parameters.

Despite this global agreement, there are characteristic differences:

- Isotopic effect

No distinct confinement difference is observed between hydrogen and deuterium discharges (in all collisionality- and ß-ranges, with T_e/T_i large or close to one). There is also no obvious isotopic dependence in the required conditions to transit into the H-mode. Therefore, the results given here are obtained with H^+ (and H^o injection). Only the details of the transition from normal confinement (NC) to the HDH-mode (see chapt.6.2) depends on the working gas.

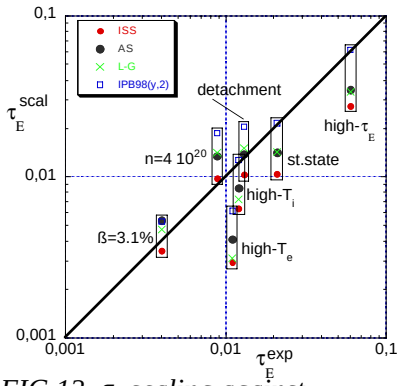

FIG.12. τ_E scaling against experimental values at operational boundaries. The W7-AS data are with hydrogen; the H-mode scaling is applied assuming deuterium

- Density scaling

Stellarators show a distinct density dependence in confinement time up to 1.5-2 10^{20} m^{-3} (lest a transition in confinement occurs). This general n_e scaling does not lose its importance in larger devices (LHD, /8/). Fig. 13 summarises the role of density on energy and impurity (aluminium) confinement. At lower densities the plasma is heated by ECRH, whereas at higher density (> 8 10^{19} m^{-3}) NBI heating has been applied. With NBI at a density beyond 1.5 10^{20} m^{-3}, the transition into the HDH regime occurs. The medium to low density cases are compared with the W7-AS- and the ISS95 scaling. In the HDH regime, the confinement is superior by a factor of 1.5 to 2. H* results are shown for comparison. Also the impurity confinement time τ_I is shown in Fig. 13; it is measured by Al-laser-blow-off. This parameter also scales with density with the consequence, that beyond n_e = 5 10^{19} m^{-3}, impurity accumulation occurs and no steady-state operation is possible. At the HDH transition, τ_I is strongly reduced and steady-state operation is recovered.

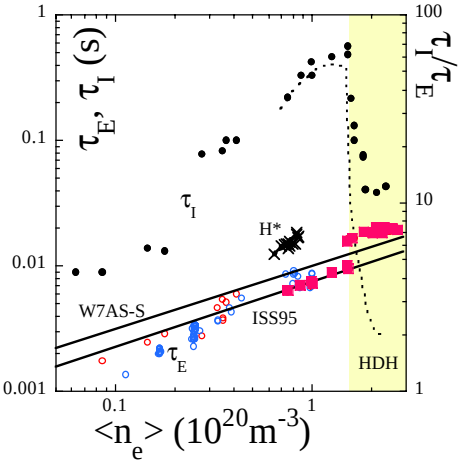

FIG. 13. Dependence of energy τ_E and impurity confinement τ_I times on the line averaged density (a_{eff} = 0.12 m; ι = 0.5, B_t = 2.5T, P = 0.65 - 0.75 MW). The transition into the HDH regime is indicated. Also the ratio τ_I/τ_E is given (dashed curve). The τ_E-values with open symbols and the H values are obtained at different a_{eff} and scaled according to the W7-AS- and ISS95-scaling ($\approx a_{eff}^{2.21}$) to allow comparison with the results at a_{eff}=0.12 m.*

- Lack of profile resilience

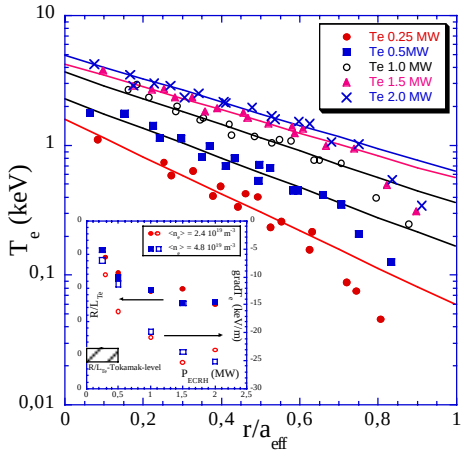

A distinct difference to the behaviour found in tokamaks but also in LHD /9/ seems to be the orthodox response of the T_e-profile to changes of the heating power and the power deposition. Off-axis heating with ECRH leads to flat (or hollow) T_e-profiles inside the deposition radius /9/.

FIG. 14. T_e-profiles for an ECRH power range from 0.25 to 2 MW; insert: T_e-gradient and R/L_{Te} versus range typical for tokamaks is indicated.

Fig. 14 shows T_e-profiles in log-representation for centrally ECRH heated electron transport dominated discharges with heating power varying from 0.25 to 2 MW at n_e=4.8 10^{19} m^{-3}. The insert shows the T_e-

gradient (mid-radius) and the parameter R/L_{Te} for two densities.

The T_e –gradient increases with heating power; R/L_{Te} is larger than in tokamaks (but the aspect ratio of W7-AS is 11) and falls with increasing power because of a strong T_e-rise in the plasma periphery. For the 2 MW case, the power flux through the mid-radius flux surface is about 0.25 MW/m^2.

Heat wave experiments by ECRH modulation yield $\chi_{HP} \approx \chi_{PB}$. Also these studies do not reveal an intrinsic transport mechanism, which is governed by turbulence-onset at a critical gradient $L_{Te,c}$. Fig. 15 shows the results from on- and off-axis power modulation. The phase of the T_e-wave drops symmetrically to the inside and the outside of the off-axis deposition radius (r/a=0.45). The T_e-profile is flat in the inside but steep in the outside. In a mixed case with on- and off-axis heating (at the same total power of 1.2 MW), χ_{HP} and χ_{PB} could be analysed. Outside the ECRH deposition both are unchanged. For r/a < 0.45 only χ_{HP} could be estimated. It rises from $1<\chi_{HP}<2.5 m^2/s$ without central heating to $4<\chi_{HP}<12$ m^2/s for 0.6 MW central ECRH power.

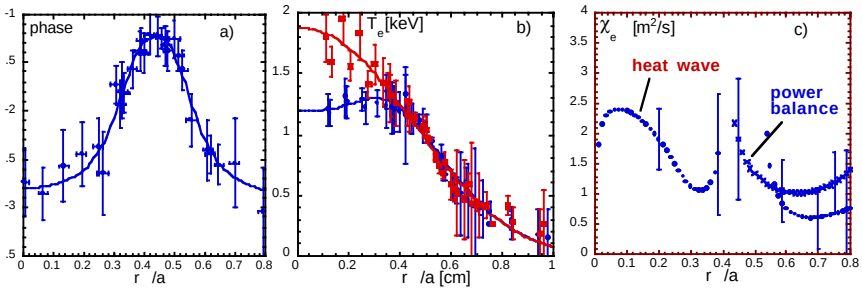

FIG.15. Left: radial variation of the heat wave phase (deposition at r/a=0.45); middle: T_e profiles (on, off axis); right: heat-wave and power balance χ_e for the case with 0.6 MW on and 0.6 MW off axis.

6. Improved confinement regimes

6.1. H-mode

In the experiment a fairly complex manifestation of the H-mode is observed, depending on the magnetic configuration, on density and heating power:

- it can develop with grassy ELMs, solitary large ELMs, with dithering and quiescent phases;
- the quiescent H-mode develops in small iota windows in the neighbourhood of ι ~ 0.5 with separatrix;
- at high density, the H-mode can develop in the form of a high-density H-mode (HDH) with good energy- and low impurity confinement;
- around ι=0.34, under limiter conditions, the H-NBI mode develops /10/. The steep gradient radius and the ELM origin are located further in;
- According to the presence of grassy ELMs, the H-mode can develop right at the beginning of the discharge without noticeable transition; the transition into the quiescent H-mode occurs at a critical (power dependent) density and has an upper power limit.

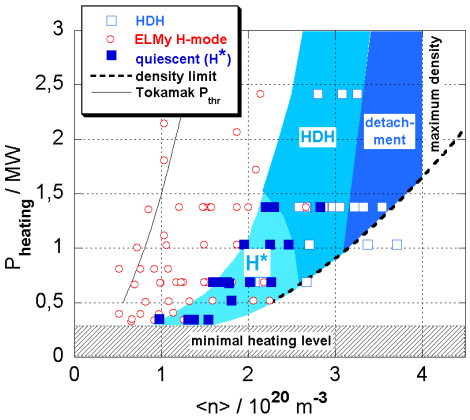

FIG. 16. Operational range of the different forms of H-modes in W7-AS. Also given are the density limit (chapt. 8.2) and the operational limits (n_e=4 10^{20} m^{-3}, P_{min} 0.25 MW) and the tokamak power threshold.

Fig. 16 shows H-mode variants in a P vs. <n_e> operational plane with 5/9 island edge conditions. H-modes have been obtained with ECRH and NBI down to the technical limits of 0.25 MW. A possible power threshold is lower than in conventional tokamaks, which, again, is lower than in spherical tokamaks /11/ possibly pointing toward an intrinsic aspect ratio scaling. The low value of W7-AS may reflect the low neoclassical damping of poloidal flow owing to the large aspect ratio. ELMy H-modes are obtained in a large parameter range. The quiescent H-mode is restricted in operational space with a tight coupling between density and power. The HDH-mode (see chapt. 6.2) can be accessed from ELMy-phases or from the H*-mode. It is restricted to high density.

The H-mode is observed only close to ι ≈1/2 under separatrix conditions. Fig. 17 is another operational diagram with density and ι. The data points show H- and L-mode plasmas and indicate the three H-mode windows. Also shown is the density limit for the heating power of 0.4 MW (chapt. 8.2). H-modes can be operated close to the density limit, which varies with ι because of the intrusion of edge islands, which modulate the plasma cross-section and with it the heating power density. Indicated are also the ranges with large poloidal viscosity due to the specific field spectrum at the edge of W7-AS. Obviously, the quiescent H-mode cannot develop in regions with low order islands at the edge and with strong poloidal damping.

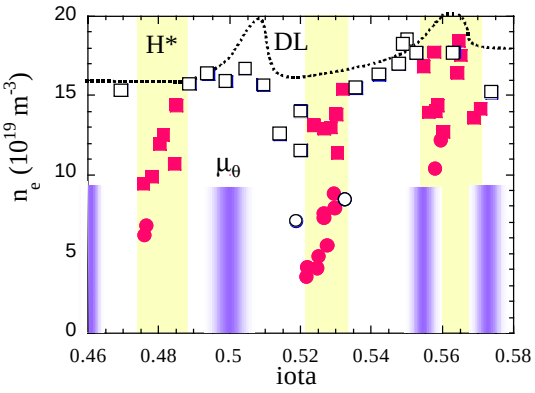

FIG 17. n_e-ι operational H-mode range. The symbols discriminate between L (open)-and H-mode (closed) plasmas. The dashed curve shows the density limit for 0.4 MW NBI). The zones of large poloidal flow damping are also indicated (bars, denoted by μ_Θ)

Fig. 18 shows the variation of the spectroscopically measured radial electric field E_r, the diamagnetic term p_i'/en_e, deduced from the local parameters, and the poloidal flow resulting from the difference between field and diamagnetic component. v_Φ is assumed to be zero. For orientation, the H_α traces are given. Both discharges develop a quiescent H-mode, (#47108 at n_e=0.7 10^{20} m^{-3}, P_{NBI}= 0.4 MW, #47121 at n_e=1.2 10^{20} m^{-3} and 1.2 MW). The independently determined E_r and p_i'/en_e agree quite well. Both develop when dithers appear and further deepen at the H*-transition. The v_θxB term is, however, small but increases toward the transition (in ion drift direction). The pressure gradient-term largely determines E_r. (Because of the uncertainty in the data, two cases at different parameters are shown).

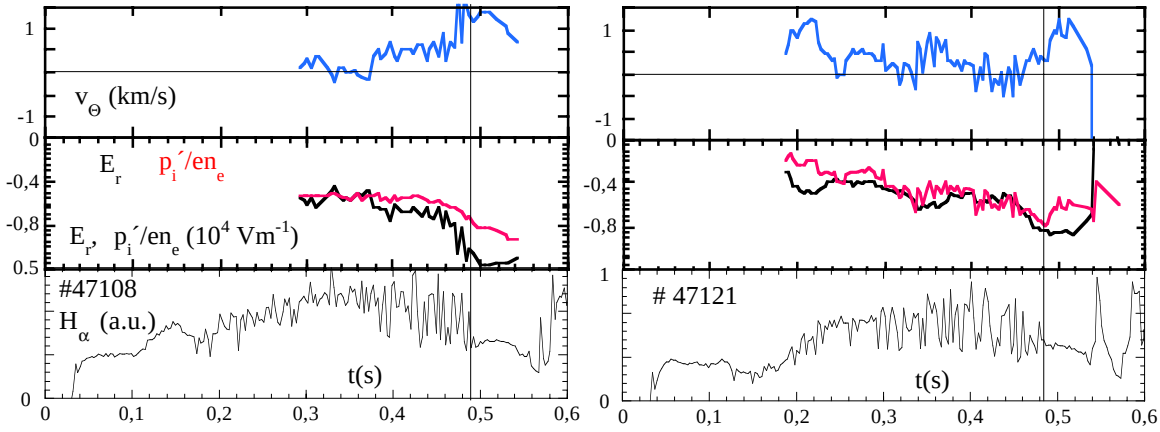

FIG. 18. H_α, E_r, p_i'/en_e, and v_Θ for H-modes with transitions into quiescent phases. Two cases at different density and beam power are shown. B_0 = 2.5 T.-

Fig. 19 expands the time scales for the transition and plots the L->H and the H->L transition (after the NBI pulse has been switched off). Plotted are again the spectroscopically measured E_r supplemented by E_r deduced from Doppler reflectometry. The poloidal propagation of turbulence is used to assess E_r. The agreement of both methods is good. The Doppler data require the presence of turbulence. Between ELMs, no signal is available.
Plotted in Fig. 19 is also the power level of the turbulence (measured with the same probing μ-wave beam at the same location). All data are taken in the vicinity of the profile pivot point from L- to H-mode. The transition into the H-mode shows a preceding phase where E_r already deepens (the absolute value of the negative E_r is plotted) and the turbulence gradually reduces. The transition occurs typically at an $E_r' = 10^3$ kV/m^2. Interesting is the back-transition. As soon as the beams are switched off at 0.6 s, $|E_r|$ decreases and the turbulence level increases and scattering signal appears. At the transition, E_r and simultaneously the fluctuation power jump

(note the logarithmic scale). In the second L-phase, the E-field still decreases, the fluctuation level increases and both saturate in the evanescent phase of the plasma. Both transitions exemplify the close correlation between E-field (E_r') and the turbulence. The H-transition occurs under conditions, which are gradually approached in the pre- and the post phase. The significance of the parameter jump at the H-to L-transition has yet to be clarified.

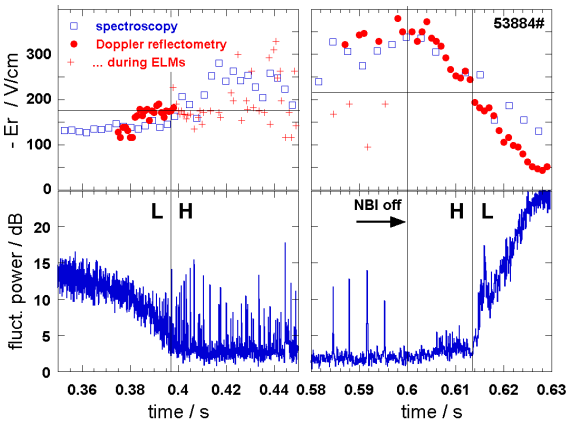

FIG. 19. E_r deduced from spectroscopy and from Doppler reflectometry and the fluctuation power (log-scale) for the L- to H-transition (left) and the H-to L-back transition (right).

6.2. High-density-H-mode

At even higher density, the dynamics of the plasma changes once more. A transition into the HDH-mode occurs (Fig. 16). This mode is accessible from the regular quiescent H-mode (H*) or from NC (either L-mode or ELMy H-mode), which is, in this high-density regime, established by NBI with rather peaked density profiles. The transition into the HDH-mode can occur from a state with peaked or a state with broad density profiles. It always ends in a state with broad density profiles. The transition requires a critical density, which itself depends on heating power (P_{abs}=0.7MW: n_e = 1.5 $10^{20}m^{-3}$, 1.4MW: n_e = 1.8 $10^{20}m^{-3}$, 2.45MW: n_e = 2.2 10^{20} m^{-3}). The main feature of the HDH mode, the broad density profile, may develop in the competition between edge and central fuelling. With beam fuelling, both forms of proceeding phases are prone to impurity accumulation, increase of core radiation and discharge collapse. As soon as the HDH-mode is reached, the impurity confinement time rapidly drops (Fig. 13) and the plasma purifies itself. In this regime, τ_E and τ_I are no longer conforming to each other. The radiation profile strongly changes from core dominated to an edge dominated radial profile. The change in energy confinement time at the transition depends strongly on the pre-phase: Starting from NC, τ_E rises at the transition (f_H≈1.7-2), starting from the H*-mode, the confinement remains about the same (Fig. 13). τ_I / τ_E ≈ 2 in HDH.

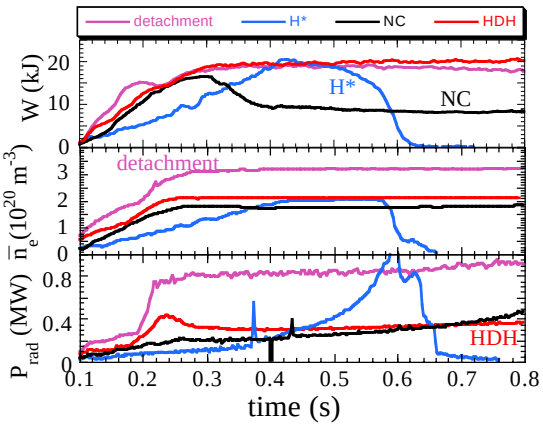

Fig. 20 shows energy content, line density and total radiation of different confinement regimes (H*, NC (ELMy H-mode), HDH, detached plasma). H* and ELMy-H-mode do not reach steady state; HDH and detached plasmas do. Under detached conditions, the edge radiation is close to 100%; the energy content does not further rise with density because detachment leads to a reduction of the effective plasma cross-section.

FIG. 20. Energy content W, line density and total radiation P_{rad} vs. time for different conditions: H, NC (ELMy H-mode), HDH and under detached conditions. P_{NBI} = 1.4 MW.*

It is difficult to understand the sudden change in impurity confinement at the HDH transition. The proton density profile plays an important role both in tokamaks and stellarators with respect to the ratio of $v_{in,imp}$/D. Qualitatively, it may be understandable that the broadening of the density profile at the transition from NC to HDH removes the impurities. Indeed, laser-blow-off (LBO) measurements show, that $v_{in,imp}(a)$ is the quantity, which changes strongly at the transition to HDH. Applying a simplified transport model [D(r)=const., $v_{in}(r)=(r/a)v_{in}(a)$], $v_{in,imp}(a)$ was found to be strongly reduced from –10 (r/a_{eff}) m/s to –2.7 (r/a_{eff}) m/s whereas D stays rather invariant at 0.1 m^2/s . The actual problem seems to be the impurity accumulation in case of H* inspite of the broad density profile.

There is no evidence of a quasi-coherent mode at the edge /12/ of HDH. The transition from H* to HDH is initiated by gas-puffing to increase the density. With the gas-puff, $|E_r|$ becomes smaller and, after a dwell-time, HDH develops, the impurity radiation drops, and the power flow onto the target plates rises (Fig. 22).
The HDH regime allows steady plasma operation and it is rather robust. This mode with good energy and bad impurity confinement can easily be established for all powers above 0.7 MW (power flux across the separatrix: 0.06 MW/m^2) and it is established for the highest ß-values achieved in W7-AS. Considering the advantages of high densities for divertor operation, the HDH-mode may be the preferred operational mode for W7-X. Then the role of the collisionality ν in its development (e.g. for the transition conditions) and further characteristics of the HDH-mode can be explored. In case a more ubiquitous character of the HDH mode emerges in the W7-X operation, it might be the favoured operational mode in the future because it combines good energy confinement and low impurity confinement without the need for ELMs.

6.3. H-NBI Mode

At ι ≈ 0.34, the other window with good confinement, the classical H-mode does not appear probably because only limiter operation is possible. In this ι-range another good confinement mode, termed the H-NBI mode /10/, develops in beam heated discharges. In this case, the steep pressure gradient does not reside at the very plasma edge but at about 2/3 a. Because of the large plasma cross-section (a_{eff} ≈ 0.18 m), the best confinement times have been observed in this regime. Also small ELMs appear with a pivot point, which is located at the minimum of p_i' and which has moved with it further in (from r_s-r_{pp} ≈1.5 cm in H* to 4.5 cm).

7. Stability

7.1. Global Alfvén Modes

In stellarator operation proper, only pressure driven instabilities develop in W7-AS - MHD modes, which are driven by the thermal pressure, and global Alfvén eigenmodes (GAE), which are driven by the fast particle pressure. Only with additional currents, driven ohmically or with ECCD, current driven instabilities are induced. At the edge, ELMs appear in the H-mode, destabilised by either the edge pressure gradient or the edge bootstrap current.

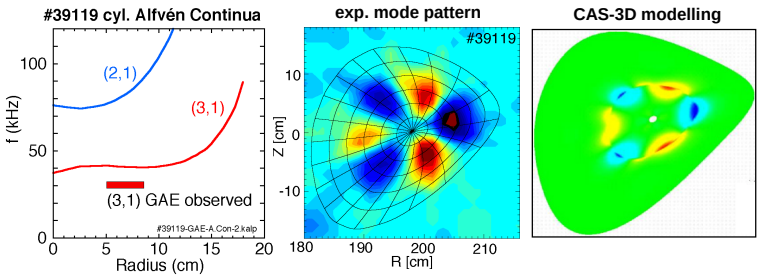

FIG. 21. m=3 GAE mode at 28 kHz measured via SX tomography; mode pattern calculated with the CAS3D code; Alfvén continuum bands with the mode location in space and frequency

Pressure driven MHD does not play a role as long as the location of the resonance in the region of steep gradients is avoided. High-ß discharges are found to be rather quiescent, because both MHD and GAE modes are stabilized (Fig. 9). Fig. 21 shows measured and computed (with CAS3D) GAE m=3 mode pattern. The mode is localised just beneath the (3,1) shear Alfvén continuum band. Only bursting high-frequency GAE modes lead to beam particle losses.

7.2. ELMs

ELMs in W7-AS have basically the same features (relative location, duration, frequency spectrum, energy loss (4%), level of power deposition onto target plates) as in tokamaks. Fig. 22a shows the power flux onto the divertor target at the transition from an L-phase into an ELMy H-mode.

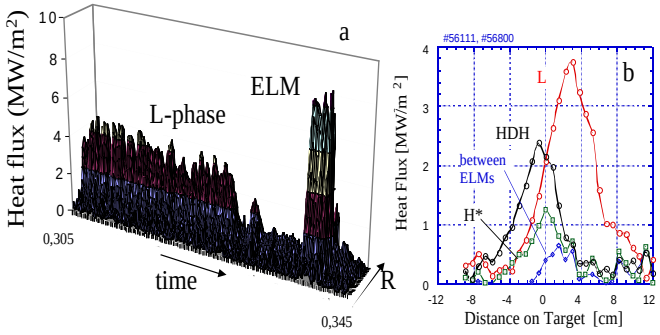

FIG. 22. Profiles of the power deposition onto the divertor target. a) at the transition from L- to ELMy H-mode; b) deposition profiles in different regimes.

ELMs give rise to power fluxes up to 20 MW/m2. Between ELMs, there is basically no power flux. Fig. 22 b shows target plate deposition profiles for various conditions – L-phase, HDH-phase, H*-phase and the flux between ELMs. The width of the profile is about the same; also the energy of an ELM is deposited at about the same profile width.
A detailed account of MHD studies on W7-AS is given in /13/.

8. Operational limits

8.1. Maximal parameters

Under separate conditions, W7-AS has achieved the following maximal parameters:

T_e = 6.8 keV	B_0 = 2.5 T; ι_a = 0,34; n_e = 2 10^{19} m^{-3}; P_{ECRH} = 2 MW
T_i = 1.8 keV	B_0 = 2.5 T; ι_a = 0,345; n_e = 5 10^{19} m^{-3}; P_{NBI} = 1.3 MW
n_e = 4 10^{20} m^{-3}	B_0 = 2.5 T; ι_a = 0,55; P_{NBI} = 2.4 MW; T_e = 0.35 keV
<ß> = 3.4 %	B_0 = 0.9 T; ι_a = 0,5; n_e = 2 10^{20} m^{-3}; P_{NBI} = 2.8 MW
τ_E = 0.06 s	B_0 = 2.5 T; ι_a = 0,345; n_e = 1.1 10^{20} m^{-3}; P_{NBI} = 0.33 MW
$n_e T_i \tau_E$ = 5 10^{21} eVsm^{-3}	B_0 = 2.5 T; ι_a = 0,345; n_e = 1.1 10^{20} m^{-3}; P_{NBI} = 0.33 MW

TABLE I. Maximal plasma parameters of W7-AS.

8.2. High-density operation and density limit

High-density operation is done with gas puff fuelling only. Successful high-density operation requires good boundary conditions (e.g. the island divertor). Fig. 23 shows the high-density discharges of W7-AS compared with the density values stored in the ITER H-mode database. The two data groups are well separated: Unlike confinement, the physics of the density limit seems to be different between tokamaks and stellarators. In W7-AS, the density limit is caused by a gradual decay of the plasma owing to excessive radiation and can numerically be described by the power balance; in tokamaks, it is given by an MHD instability. No disruptive density limit has been observed in W7-AS operation up to the ß limit. The density limit of W7-AS follows the scaling: $n_{e,pred}$ = 1.462 $(P/V)^{0.48}$ $B^{0.54}$ (MW, T, $10^{20}$$m^{-3}$).

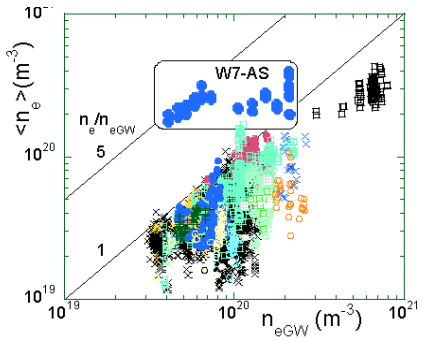

FIG. 23. Density limit values of W7-AS compared to the density values of the ITER H-mode data base plotted against the Greenwald density limit (current is replaced as described above).

8.3. ß-limits

The maximal <ß> values in W7-AS of up to 3.4% were still power and not MHD limited. The maximal core values reach up to 7%. Maximal ß´s are obtained with 0.9 T < B_0 < 1.25 T. The core of the high-ß plasma is in the plateau-regime. Fig. 24 shows the maximal <ß> values in comparison to those of the ITER database. The two data groups are well separated. Like the density limit and different to confinement, also the mechanisms which limit <ß> seem to be different in W7-AS and tokamaks. A detailed account of ß-limit studies is given in /13/.

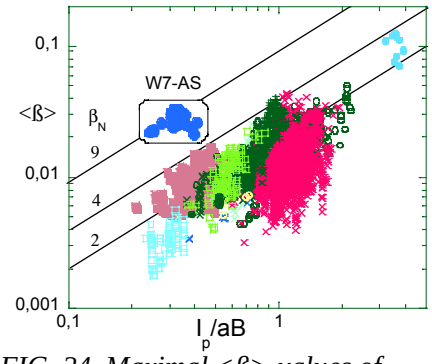

FIG. 24. Maximal <ß>-values of W7-AS compared with the ß-values of the ITER H-mode data base.

9. Steady-state operation

Unlike W7-X, W7-AS is not equipped with superconducting coils. The potential for steady-state operation can only be demonstrated in short pulses and the observed impurity properties. Fig. 25 shows a high-density long-pulse divertor discharge at different power levels. Despite the high density, the impurity radiation remains at the plasma edge; no impurity accumulation

is observed. The SOL mid-plane density is typically 3-8 10^{19} m^{-3}; the neutral pressure inside the divertor is about 10^{-3} mbar, sufficient for particle control. The ratio of impurity- to energy confinement time can be as small as 2, which fulfils the general target for ignition (<5). The Greenwald factor $n/n_{GW} \approx 1$; the confinement H-factor ≈1 (related to the ITER ELMy H-mode scaling).
Fig. 26 shows a quasi-steady-state high - ß discharge with quiescent termination.

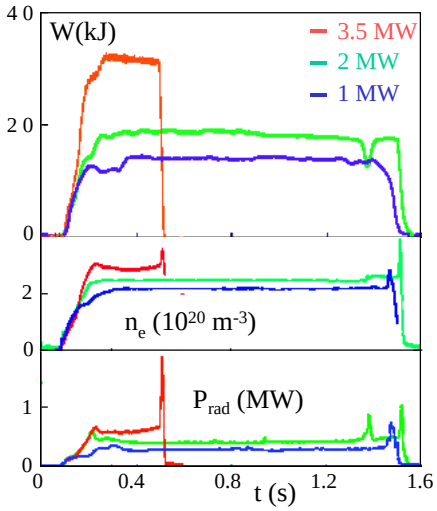

FIG. 25. Long-pulse discharges at different NBI powers. B_t = 2.5 T

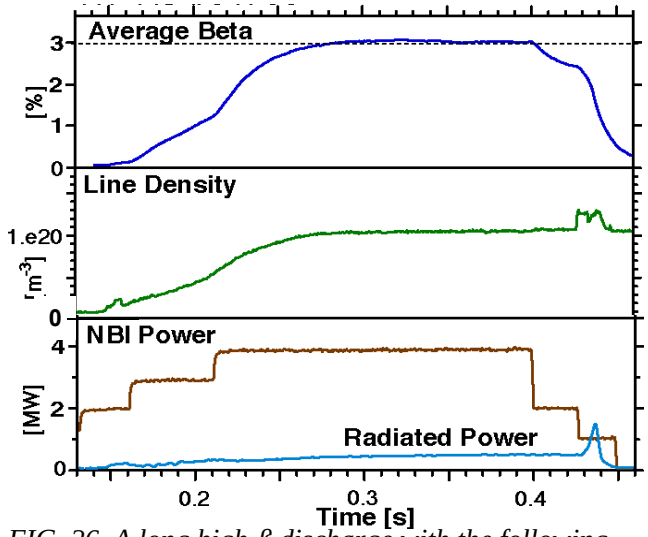

FIG. 26. A long high-ß discharge with the following parameters: $q \approx 2$, $\kappa \approx 1.9$, $n/n_{GW} \approx 3.1$, $ß_N \approx 8.4$, $\tau_E/\tau_E^{89} \approx 2$, $\tau_E/t_{ft} \approx 30$

10. Conclusions

W7-AS has fulfilled its major goals
- to test the modular coil concept
- to develop the island divertor
- to test the effectiveness of the first steps in stellarator optimisation and thus to contribute to the scientific basis for W7-X
- to contribute to the physics of toroidal confinement and to stellarator physics.

In W7-AS divertor operation was possible with good plasma confinement under quasi-steady-state conditions in an ELM-free variant of the H-mode. The H-mode power threshold is low. Also close to operational limits, the plasma performance is found to be free of violent instabilities. The heating power limited ß-values are high. Operation at high densities was possible. The plasma performance does not noticeably decline close to limits. W7-AS operation has contributed to further establish the Wendelstein stellarator concept as an independent reactor line.

References

/1/ Y Feng, F Sardei, et al., Plasma Phys. Control. Fusion 44 (2002) 611
/2/ J. Preinhaelter and V., Kopecky, J. Plasma Phys. 10, 1 (1973)
/3/ V. Erckmann, et al., this conference; and references therein.
/4/ D.A. Hartmann et al., 27th EPS Conf. Contr. Fusion Plasma Phys., Budapest 2000, ECA Vol. 24B (2000),5-8
/5/ U. Stroth, et al., Nuclear Fusion 36, 1036 (1996)
/6/ R. Brakel, et.al., this conference; and references therein.
/7/ K. Yamazaki et al., 13th IAEA-Conf. on Fusion Energy, Sorrento, 2000
/8/ N. Ohyabu et al., Plasma Phys. Contr. Fusion 44, A211 (2002)
/9/ F. Wagner et al., Phys. Rev. Letters, 56, 2187 (1986)
/10/ U. Stroth et al., Plasma Phys. Contr. Fusion 40, 1551 (1998)
/11/ A.R. Field et al., Plasma Phys. Contr. Fusion 44, A113 (2002)
/12/ M. Greenwald et al., Plasma Phys. Contr. Fusion 42, A263 (2000)
/13/ A. Weller et al., this conference; and references therein.